

Continuous wave spectroscopy of nonlinear dynamics of Si nanocrystals in a microdisk resonatorMin Xie,^{1,2} Alessandro Pitanti,³ Mher Ghulinyan,^{4,*} Deren Yang,² Georg Pucker,⁴ and Lorenzo Pavesi¹¹*Nanoscience Laboratory, Department of Physics, University of Trento, via Sommarive 14, IT-38123 Povo (Trento), Italy*²*Department of Materials Science and Engineering, State Key Laboratory of Silicon Materials, Zhejiang University, Hangzhou 310027, China*³*NEST, Scuola Normale Superiore and Istituto Nanoscienze-CNR, piazza S. Silvestro 12, IT-56127 Pisa, Italy*⁴*Advanced Photonics and Photovoltaics group, Fondazione Bruno Kessler, via Sommarive 18, IT-38123 Povo (Trento), Italy*

(Received 12 July 2011; revised manuscript received 20 October 2011; published 15 December 2011)

We report on a study of the recombination dynamics of silicon nanocrystals (Si-ncs) embedded in a planar whispering-gallery mode resonator. Fundamental properties of exciton dynamics in Si-ncs, in particular their absorption cross-section and excited carrier-related losses, can be extracted from continuous-wave spectroscopy by analyzing the resonance linewidths at different excitation powers. Observation of nonlinear drifts of mode peak positions in the same experiment allows us to model the nonlinear refractive index of the nanocrystalline material. The theoretical results confirm that the observed sublinear blue and linear redshifts of resonance peak positions are induced by excited carrier effects and thermal heating at low and high pump powers, respectively. The extracted thermo-optic coefficient, $k_T = 1.46 \times 10^{-4} \text{ K}^{-1}$, and excited carrier refraction, $k_{EC} = -1.07 \times 10^{-23} \text{ cm}^3$, in Si-ncs, are of relevance since they may induce important modulation of the fine modal structure of an optically active cavity.

DOI: [10.1103/PhysRevB.84.245312](https://doi.org/10.1103/PhysRevB.84.245312)

PACS number(s): 42.55.Sa, 78.67.Bf, 78.20.N-

I. INTRODUCTION

Optically active photonic devices which exploit the properties of silicon nanocrystals (Si-nc) are of interest since they enable new functionalities or phenomena in silicon photonics.¹ In the last years particular interest has been raised for studying the optical properties of Si-ncs embedded in a whispering-gallery mode (WGM) resonator. Experiments allowed observation of light emission at near-infrared (NIR) wavelengths with characteristic modal features from optically pumped microresonators.^{2,3} Analysis of the principal loss mechanisms in microdisk resonators has been carried out,⁴ and the tuning of the quality factors (Q) of mode emission has been achieved by using exotic resonator shapes.⁵ In addition, coupling of Si-ncs emission to WGM resonances of a low-loss silica ring resonator⁶ and Purcell enhancement of the emission rates of Si-ncs⁷ have all been demonstrated.

A general property of these devices is that within the NIR light-emission band of Si-ncs the obtainable Q s are only of the order of several thousands. This fact is mainly associated with the strong increase of optical losses due to excited carrier absorption (ECA).^{3,4} In fact, a photoexcited carrier in a Si-nc can further absorb the light generated by exciton recombination in Si-ncs. This reabsorption generates additional material losses, and, when the Si-ncs are embedded in a cavity, it increases the mode loss, limiting, therefore, the cavity Q .

In this paper we present a systematic study of NIR light emission from Si-nc-based WGM resonators. We show that by analyzing the excitation pump intensity-dependent emission from resonator modes several pieces of information on Si-ncs embedded in the WGM resonator can be revealed. In particular, the excitation cross section of Si-ncs can be obtained from the study of the power variation of the quality factors. Moreover, the nonlinear refractive index can be obtained by modeling of the spectral shifts of WGM resonances versus the pump power. The model includes contributions both from ECA and thermal heating. Typically, these quantities

in a bulk nanocrystalline material [silicon-rich oxide (SRO)] are obtained through complicated experimental arrangements (pump-probe, Z -scan, etc.), which require high temporal resolution. We demonstrate, in this study, that the same parameters can be obtained based on simple continuous-wave (CW) photoluminescence (PL) experiments.

The paper is organized as follows. In Sec. II we describe the experimental technique and provide the characteristic PL spectra of studied Si-nc-based WGM resonators. In Sec. III we discuss the cavity loss mechanisms, model the ECA-related loss, and, based on it, analyze the experimental data. In Sec. IV we address the nonlinearities in the SRO material, model the experimentally observed peak shifts, and extract the nonlinear coefficients related to the thermo-optic and excited carrier refraction effects. Finally, in Sec. V we summarize our results and draw some conclusions.

II. EXPERIMENTAL RESULTS**A. Sample fabrication**

Suspended Si-nc-based planar microdisk resonators of $10 \mu\text{m}$ in diameter have been realized following the method described in Ref. 3. In particular, the microdisk fabrication starts with a deposition of a 250-nm-thick SiO_x layer on top of crystalline silicon wafers from a mixture of silane (SiH_4 , 65 sccm) and nitrous oxide (N_2O , 973 sccm) gases using a parallel-plate plasma enhanced chemical vapor deposition (PECVD) chamber at 300°C . A successive one-hour annealing in a nitrogen atmosphere at 1100°C results in the formation of Si-ncs (through a phase separation process of SRO into Si and SiO_2) embedded in a silica host. During this thermal treatment the SRO layer densifies down to 200 nm due to the release of hydrogen and microvoids, present in the as-deposited layer. Then, a photolithographical patterning of microdisk arrays is performed and followed by dry (anisotropic, SRO disk definition) and selective wet etching (isotropic, Si pedestal) steps. Finally, the photoresist is removed in an O_2 -plasma

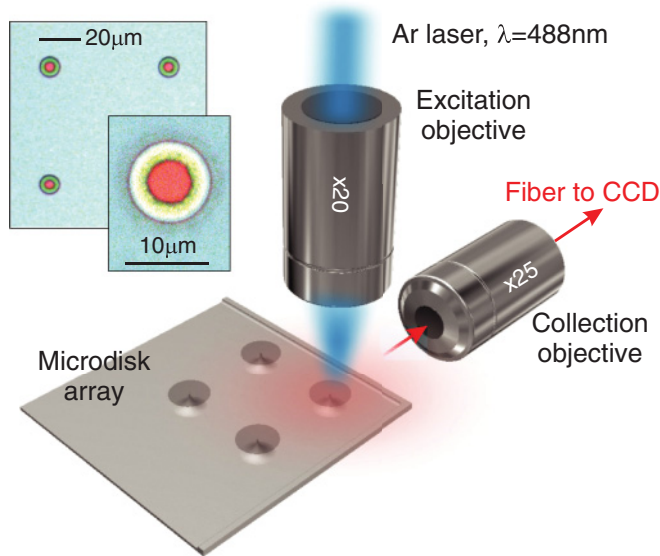


FIG. 1. (Color online) A three-dimensional sketch of the experimental setup and measurement configuration. A top-view optical micrograph of the sample and the zoom of a 10- μm -diameter microdisk resonator are also shown in the upper left corner.

chamber. By the end of the described fabrication steps, monolithic Si-nc-based suspended microdisk resonators are realized.

B. WGM emission from active resonators

The resonators were studied under CW excitation (Ar⁺ laser, excitation wavelength $\lambda_{\text{exc}} = 488 \text{ nm}$) using a microphotoluminescence (micro-PL) setup, which is sketched in Fig. 1. A fiber-coupled monochromator with a CCD detector is used to analyze the emission spectra. Critical for the measurements are the excitation of a single microdisk and the observation of the emission in the plane of the microdisk with a small numerical aperture collection optics.³ The polarization of the collected emission was also selected [transverse electric (TE) indicates that the electric field is in the microdisk plane, and transverse magnetic (TM) indicates that the magnetic field is in the microdisk plane].

A typical TE-polarized PL spectrum is characterized by narrow WGM resonances emerging from the broad emission band of Si-ncs. The broad emission is due to photons emerging from the microdisk which are not coupled to any cavity mode (placed, for example, close to the disk center). Figure 2 shows an example of such a spectrum from a 10- μm -diameter microdisk. Finite element method (FEM) numerical simulations allow identification of various cavity modes, which can be classified by the number of electrical field antinodes along the radial (p) and azimuthal ($2m$) directions, respectively, as well as their polarization state. Each WGM is labeled as $\text{TE}_{p,m}$; examples are shown in Fig. 2.

An intriguing possibility is to extract quantitative information about the Si-ncs by simple CW PL experiments. Figure 3 shows a two-dimensional map of the PL for different pump powers and wavelengths. Here the WGMs appear as narrow and intense lines. While this map is useful to identify the different radial families, quantification of excitation-induced

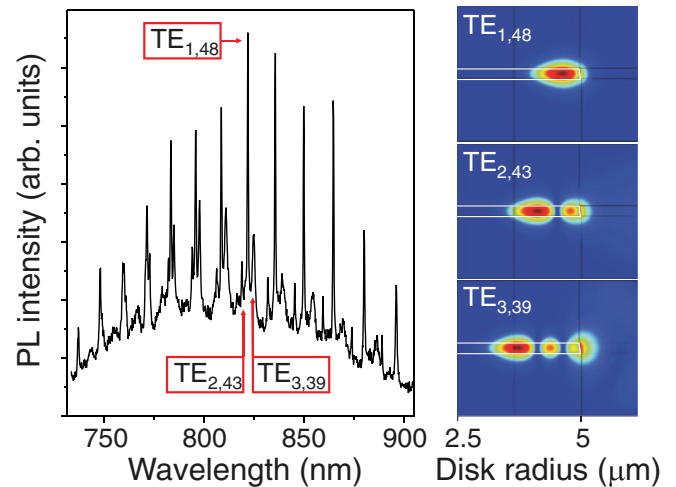


FIG. 2. (Color online) A characteristic Si-nc WGM emission spectrum from a 10- μm -diameter microdisk, where different radial WGM families can be identified. As an example, a few are labeled with the polarization and radial and azimuthal mode numbers. On the right panel the calculated electric-field intensity profiles of modes labeled in the emission spectrum (wavelength $\simeq 825 \text{ nm}$) are reported. The white contours visualize the microdisk cross section.

losses and nonlinear effects in Si-ncs can be inferred through a careful analysis and modeling of the WGM line broadening, as well as the spectral shifts. This will be done in the next sections.

III. RESULTS AND DISCUSSION

A. Excited carrier absorption

Pump-probe experiments (with a 1.5 μm wavelength probe, a 532 nm excitation pump with a photon flux, Φ , of the order of $10^{20} \text{ ph.}/(\text{cm}^2\text{s})$) have shown that the excitation-induced losses due to the ECA in an SRO waveguide can be as

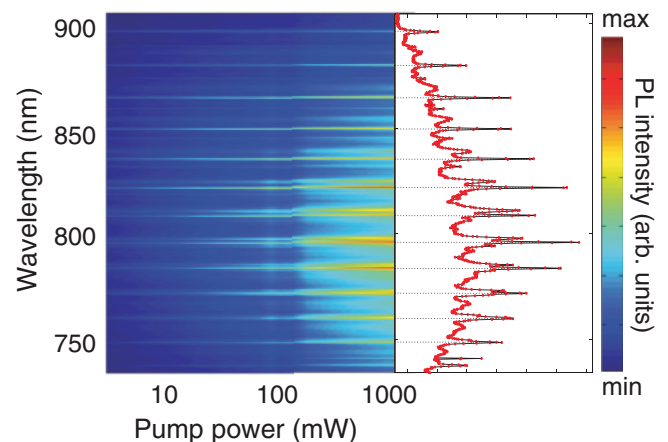


FIG. 3. (Color online) The PL intensity map vs excitation power ($\lambda_{\text{exc}} = 488 \text{ nm}$) and wavelength obtained from a 10- μm microdisk. The color bar refers to the PL intensity in arbitrary units. It is worth noting that the peak-to-background contrast increases at large pump powers, allowing an easy recognition of several high-order families. On the right panel the PL spectrum obtained at 1 W pumping power is reported.

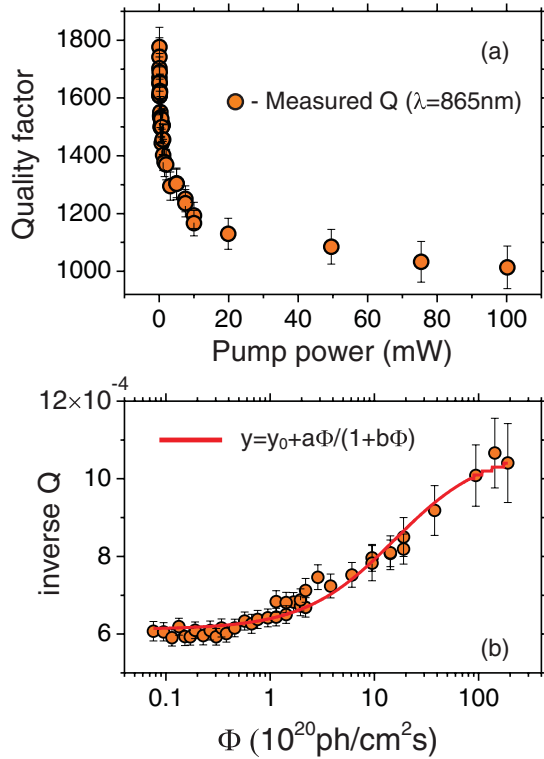


FIG. 4. (Color online) (a) The mode quality factor vs pumping power for the WGM at 865 nm. (b) The inverse of Q vs the incident photon flux (Φ). The line is a fit to the data with a sigmoidal function $y = a\Phi/(1 + b\Phi)$.

high as 1.38 cm^{-1} .⁹ Such a value represents an important nonlinear loss mechanism in Si-nc-based optical device. A characterization of ECA at NIR wavelengths can be obtained by analyzing the spectral linewidths of the microdisk. In fact, the quality factor of a WGM mode, which is inversely related to the cavity loss, can be evaluated by the ratio of the peak frequency and spectral full width at half maximum of the Lorentzian-shaped resonance. When this is applied to various modes, shown in Fig. 3, a monotonically decreasing Q with increasing excitation pump power is observed. An example is shown in Fig. 4(a), where the Q extracted for the WGM resonance at $\lambda = 865 \text{ nm}$ is reported.

The inverse of the mode Q represents the total cavity loss (Q_{tot}^{-1}) and accounts for all possible loss channels:

$$Q_{\text{tot}}^{-1} = Q_{\text{rad}}^{-1} + Q_{\text{mat}}^{-1} + Q_{\text{ss}}^{-1} + Q_{\text{sa}}^{-1} + \dots, \quad (1)$$

where Q_{rad} accounts for the radiative losses, Q_{mat} accounts for the material losses, Q_{ss} accounts for the surface scattering, and Q_{sa} accounts for the surface absorption. For the microdisk, a good estimation of Q_{tot} can be obtained by considering only the first two terms in the right-hand side of Eq. (1).³ In particular, while Q_{rad} depends only on the cavity geometry, Q_{mat} is largely influenced by excitation power-dependent contributions. Since absorption in SRO is given by a constant term, α_0 , and an excitation photon flux-dependent term, α_{Φ}^* ,³ then we have $Q_{\text{mat}}^{-1} = \Gamma\lambda(\alpha_0 + \alpha_{\Phi}^*)/(2\pi n_{\text{eff}})$ for the material loss. Here, n_{eff} is the effective (modal) index, λ is the wavelength, Γ is the optical confinement factor, and α is the loss coefficient. This

leads to a final expression for Q_{tot} :

$$Q_{\text{tot}}^{-1} = \left(Q_{\text{rad}}^{-1} + \frac{\Gamma\lambda\alpha_0}{2\pi n_{\text{eff}}} \right) + \frac{\Gamma\lambda\alpha^*(\Phi)}{2\pi n_{\text{eff}}}, \quad (2)$$

where $\alpha^*(\Phi)$ is related to the ECA loss, α_{ECA} . Modeling of this last requires a suitable description of the exciton population dynamics in Si-ncs. The exact modeling of α_{ECA} and, therefore, N_{exc} requires solving the full rate equation Eq. (9) (see Sec. III B). For this, apart from the nontrivial power functions of ϕ involved in its analytical solution, many material-related parameters, such as the excitation cross section, the recombination lifetime, and the Auger recombination coefficient, have to be known. Due to the error of the experimental Q factors, the various material-related parameters can be fitted with rather large uncertainties. In view of this, at this stage of modeling we rely on a simplified model,⁸ in which Auger effects are not directly included but are considered as a limitation on the maximum number of excitons in the system.

Auger recombination is one of the dominant loss mechanisms in excited Si-ncs. Therefore, within a two-level model for a Si-nc, the steady-state exciton population N_{exc} can be approximated to^{8,9}

$$N_{\text{exc}} = \frac{\sigma_{\text{exc}}\Phi N_{\text{Si-nc}}}{\sigma_{\text{exc}}\Phi + 1/\tau_{\text{PL}}}, \quad (3)$$

where $N_{\text{Si-nc}}$ is the concentration of Si-ncs, σ_{exc} is the absorption cross section, and τ_{PL} is the exciton recombination lifetime. Within this approximation,

$$\alpha_{\text{ECA}} = \sigma_{\text{ECA}} N_{\text{exc}}(\Phi) = \frac{\sigma_{\text{ECA}}\sigma_{\text{exc}}N_{\text{Si-nc}}\tau_{\text{PL}}\Phi}{1 + \sigma_{\text{exc}}\tau_{\text{PL}}\Phi}. \quad (4)$$

By substituting in Eq. (2) the loss coefficient α_{Φ}^* with Eq. (4) one can show that Q_{tot}^{-1} is described by a sigmoidal function $y = y_0 + a\Phi/(1 + b\Phi)$. A fit to the Q data [Fig. 4(b)] with a sigmoidal function allows extraction of the best-fit values for a and b parameters. With simple algebra,

$$\sigma_{\text{ECA}} N_{\text{Si-nc}} = \frac{a}{b} \frac{2\pi n_{\text{eff}}}{\lambda\Gamma}, \quad (5)$$

$$\sigma_{\text{exc}} = \frac{b}{\tau_{\text{PL}}}. \quad (6)$$

The n_{eff} and Γ can be calculated by FEM simulations, while τ_{PL} were measured by time-resolved PL experiments in the bulk material.⁷ We note here that, while for the PL lifetime, τ_{PL} , one should consider also a possible shortening (with respect to the bulk lifetime) due to the Purcell enhancement at the cavity resonant wavelengths by up to $\sim 70\%$ (see Ref. 7), this modification of σ_{exc} is small with respect to the overall experimental error. Therefore, in this study the impact of the Purcell effect on τ_{PL} was neglected in a first-order approximation. Thus, it is possible to extract $\sigma_{\text{ECA}} N_{\text{Si-nc}}$ and σ_{exc} from the best-fit parameters a and b .

The results of this modeling are summarized in Fig. 5, where we report the spectral dependence of σ_{exc} measured with $\lambda_{\text{exc}} = 488 \text{ nm}$. For comparison, some values reported in the literature have been added.¹⁰ Our extracted values are compatible with the data from the literature. In the inset of Fig. 5 the spectral dependence of $\sigma_{\text{ECA}} N_{\text{Si-nc}}$ is reported. Even if a definite value for the ECA cross section is not possible to extract, since the

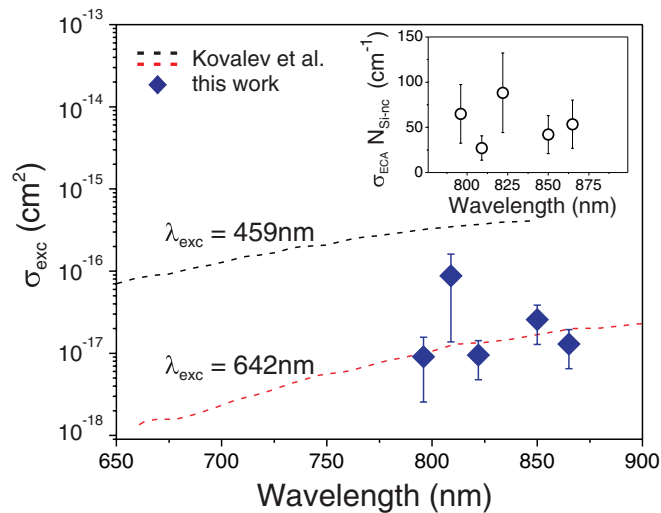


FIG. 5. (Color online) The spectral dependence of extracted σ_{exc} . The dashed curves are from Ref. 10. (Inset) The $\sigma_{\text{ECA}} N_{\text{Si-nc}}$ is plotted vs the wavelength.

Si-nc concentration is only roughly estimated, it is still possible to see that ECA-related losses represent a strong contribution in the Q reduction for the experimental excitation fluxes we have employed.

Finally, it is interesting to note that, when the exciton population saturates due to Auger effects (generating roughly one exciton per nanocrystal), the ECA loss becomes a constant term, as it appears from Eq. (4). Therefore, even at very large excitation powers, a minimum Q of about 1×10^3 is achieved in the investigated microdisk resonators.

B. WGM peak shift and optical nonlinearities in SRO

A detailed analysis of the resonant peak positions as a function of excitation intensity has been performed for several first-order radial family modes.¹¹ Figure 6 shows a three-dimensional plot of the relative peak shift, $\Delta\lambda(\Phi) = \lambda_0 - \lambda(\Phi)$, for azimuthal mode orders ranging from $m = 45$ to 51 (λ_0 is the peak wavelength for vanishingly low photon fluxes).

The plotted results show that two concurrent nonlinear effects are at work: the first one produces a blueshift of resonances and dominates at low pump fluxes, while the second one rules at large fluxes and produces a redshift. This behavior is observed for all the analyzed modes and extends over a spectrum of at least 100 nm centered around $\lambda = 800$ nm. We note that the spectral positions of resonances are fully recovered once the pump power is reduced back to its lowest level (not shown here). This indicates that no irreversible change (e.g., laser-induced oxidation) occurs in the refractive index of the cavity modes under the highest pump powers employed in the experiments. Therefore, we suggest that the various peak shifts result from the interplay of thermo-optic and free-carrier refraction effects.¹²⁻¹⁴

The refractive index of SRO can be modeled as $n = n_0 + \Delta n(T, N_{\text{exc}})$, where T is the temperature. In this way, the refractive index variation $\Delta n = k_T \Delta T + k_{\text{EC}} N_{\text{exc}}$, where k_T and k_{EC} are the thermo-optic and excited-carrier coefficients. In our experiments, we have analyzed the wavelength shift,

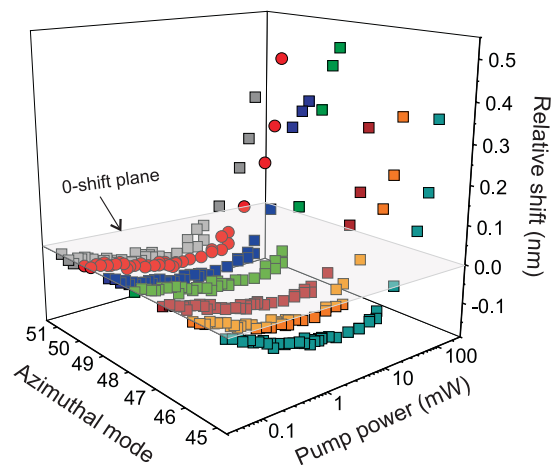


FIG. 6. (Color online) Experimentally observed shift of the cavity resonances of the first radial mode family as a function of pump power. The blueshift at relatively low powers is gradually transforming into a redshift at higher pump intensities.

$\Delta\lambda$, of the WGM modes, which reflects the variation of the mode refractive index, n_{eff} . This last, in its turn, is closely related to the material refractive index.¹⁵ Relating $\Delta\lambda$ to Δn_{eff} for cavity resonant wavelengths yields

$$\Delta\lambda(\Phi) = \frac{2\pi R}{m} (k_T \Delta T + k_{\text{EC}} N_{\text{exc}}), \quad (7)$$

where R is the radius of the resonator and m is the azimuthal mode number.

The SRO is a composite material; its large nonlinear electronic properties are given by the nanocrystalline phase (Si-ncs) both in the visible¹⁶ and in the near infrared.¹⁷ The silica host plays an important role in the heat dissipation processes. Some of these aspects have been addressed in the recent literature. The thermo-optic coefficient of SRO has been studied at $1.53 \mu\text{m}$, and we find k_T values between those of silica and of silicon.¹⁸

To get an estimate of k_T and k_{EC} from a fit of $\Delta\lambda(\Phi)$, it is necessary to relate T and N_{exc} with Φ itself. This is done here by solving the rate equations:

$$\frac{d\Delta T}{dt} = -\frac{P_A}{\rho C V} - \frac{\Delta T}{\tau_T}, \quad (8)$$

$$\frac{dN_{\text{exc}}}{dt} = \sigma_{\text{exc}} N_0 \phi - \frac{N_{\text{exc}}}{\tau} - C_A N_{\text{exc}}^3, \quad (9)$$

where P_A is the absorbed power; ρ , C , V , and τ_T are, respectively, the density, the thermal capacity, the resonator volume, and the temperature decay time constant;¹³ and σ_{exc} , N_0 , τ , and C_A are the absorption cross section, the number, the recombination lifetime, and the Auger coefficient of silicon nanocrystals. These parameters have been taken from recently reported experiments.^{19,20}

Equation (9) can be also expressed in terms of absorbed power. Considering that $P_A = \sigma_{\text{exc}} N_0 t P_{\text{IN}} = \sigma_{\text{exc}} N_0 t \phi \hbar \omega S$, where P_{IN} is the incident pump power, $\hbar \omega$ is the pump photon energy, t and $S = \pi R^2$ are the microdisk thickness and the surface area, respectively, Eq. (9) takes the form

$$\frac{dN_{\text{exc}}}{dt} = \frac{P_A}{\hbar \omega V} - \frac{N_{\text{exc}}}{\tau} - C_A N_{\text{exc}}^3. \quad (10)$$

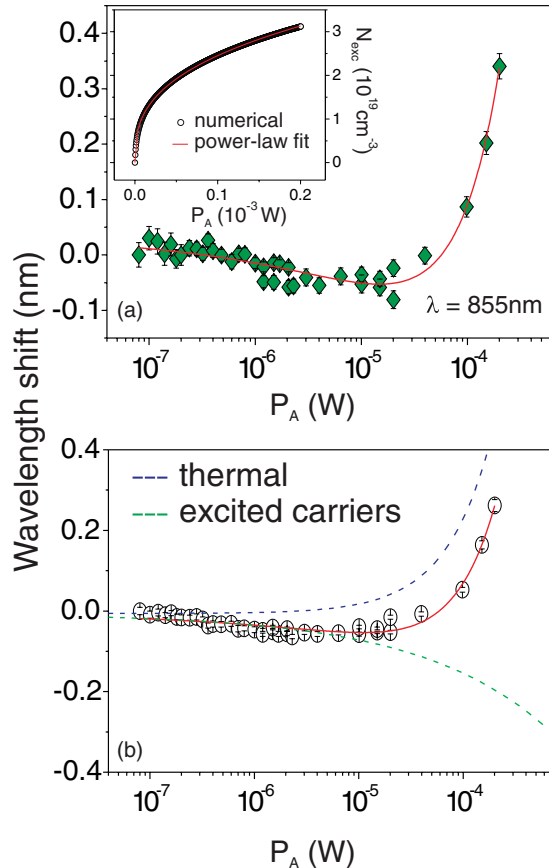


FIG. 7. (Color online) (a) Best fit of the relative peak shift of the WGM at $\lambda = 855$ nm as a function of the absorbed power P_A . (Inset) The numerically calculated exciton population N_{exc} as a function of P_A (circles) and its power law fit (line). (b) Experimental data as in (a), plotted together with separately calculated contributions from thermo-optic and electronic refractive effects.

Since the measurements are performed in CW conditions, Eqs. (8) and (10) can be solved under steady-state conditions. While the temperature variation has a simple algebraic solution, the analytic solution for N_{exc} is rather cumbersome. For this last, another possibility is to solve Eq. (10) numerically and, afterwards, fit it with an allometric power function $N_{\text{exc}} = a_1 P_A^{b_1}$ in order to obtain a manageable analytic form. The inset of Fig. 7(a) reports the obtained numerical results (scatter) and the best-fit curve (line). In particular, we obtained $a_1 = 6.351 \times 10^{20}$ and $b_1 = 0.35345$, with a coefficient of determination $r^2 = 0.9992$. Note that the power coefficient b_1 carries the signature of the recombination processes strongly dominated by the Auger mechanism within Si-ncs.²² Therefore, Eq. (7) can be reduced phenomenologically to

$$\Delta\lambda = \frac{2\pi R}{m} (k_T^* P_A + k_{\text{EC}}^* P_A^{b_1}), \quad (11)$$

where $k_T^* = -k_T \frac{\tau_T}{\rho C V}$ and $k_{\text{EC}}^* = a_1 k_{\text{EC}}$.

Equation (11) can be used to fit the data of Fig. 6. As an example, in Fig. 7(a) we report the best fit ($r^2 = 0.984$) to the experimental data for the cavity resonance at $\lambda = 855$ nm. Two different regimes can be clearly distinguished: at low fluxes, the excited carrier effects dominate, with a characteristic blueshift of the resonances. At higher excitation fluxes, the temperature-related nonlinearities start to rule out the excited carrier contribution, imposing a net redshift of the WGM peaks.

The best-fit parameters obtained are $k_T = 1.46 \times 10^{-4} \pm 2.4 \times 10^{-5} \text{ K}^{-1}$ and $k_{\text{EC}} = -1.07 \times 10^{-23} \pm 3.7 \times 10^{-24} \text{ cm}^3$. As expected, the coefficients have opposite signs and, thus, lead respectively to red/blueshifts of the resonances. In the limited spectral range analyzed here, no particular spectral trend of the coefficients can be found; the values reported here represent an average between the different analyzed modes. The evaluated thermo-optic coefficient is in agreement with the numbers reported in the literature.¹⁸ Naturally, the SRO, being a composite material (Si-ncs in a silica host), shows a lower k_T with respect to that of bulk crystalline silicon ($k_T^{\text{Si}} \approx 1.86 \times 10^{-4} \text{ K}^{-1}$). On the other hand, the excited carrier-related coefficient is two orders of magnitude lower than the free-carrier coefficients found in Si. This is particularly interesting and could be explained in terms of the spatial confinement of the excited carriers in the Si-ncs.⁹

IV. CONCLUSIONS

In conclusion, we presented a continuous-wave spectroscopic study of nonlinear dynamics of Si-ncs embedded in a planar WGM microresonator. We show that important information on fundamental properties of exciton dynamics in Si-ncs can be extracted by analyzing the excitation pump dependence of the CW emission. Both the power dependencies of resonance quality factors (thus, related cavity losses) and the peak positions can be modeled to provide an estimation of important material parameters. Our results confirm that excited carrier effects and thermal heating are competing effects in Si-nc which influence their recombination dynamics. In particular, at low power the excited carrier effects dominate, while at high pump power the thermal effects are more important. The proposed approach of analysis of the experimental data can be also extended to other material systems on which active WGM microresonators are based.

ACKNOWLEDGMENTS

M. X. acknowledges funding from the National Basic Research Program of China (973 Program, Grant No. 2007CB613403). A. P. acknowledges funding from Regione Toscana through project PORFOCUS.

*ghulinyan@fbk.eu

¹L. Pavesi and R. Turan, *Silicon Nanocrystals: Fundamentals, Synthesis and Applications* (Wiley-Verlag, Berlin, 2010).

²R.-J. Zhang, S.-Y. Seo, A. P. Milenin, M. Zacharias, and U. Gösele, *Appl. Phys. Lett.* **88**, 153120 (2006).

- ³M. Ghulinyan, D. Navarro-Urrios, A. Pitanti, A. Lui, G. Pucker, and L. Pavesi, *Opt. Express* **16**, 13218 (2008).
- ⁴R. D. Kekatpure and M. L. Brongersma, *Nano Lett.* **8**, 3787 (2008).
- ⁵M. Ghulinyan, A. Pitanti, G. Pucker, and L. Pavesi, *Opt. Express* **17**, 9434 (2009).
- ⁶B. Redding, T. Creazzo, E. Marchena, S. Shi, and D. W. Prather, *Opt. Lett.* **34**, 1384 (2009).
- ⁷A. Pitanti, M. Ghulinyan, D. Navarro-Urrios, G. Pucker, and L. Pavesi, *Phys. Rev. Lett.* **104**, 103901 (2010).
- ⁸R. G. Elliman, M. Forcales, A. R. Wilkinson, and N. J. Smith, *Nucl. Instrum. Methods Phys. Res. B* **257**, 11 (2007).
- ⁹D. Navarro-Urrios, A. Pitanti, N. Daldosso, F. Gourbilleau, R. Rizk, G. Pucker, and L. Pavesi, *Appl. Phys. Lett.* **92**, 051101 (2008).
- ¹⁰D. Kovalev, J. Diener, H. Heckler, G. Polisski, N. Künzner, and F. Koch, *Phys. Rev. B* **61**, 4485 (2000).
- ¹¹Here, with the term radial family is intended a group of quasideigenmodes with the same number of field antinodes along the radial direction. The first radial family modes possess a single antinode along the radial direction.
- ¹²R. A. Soref and B. R. Bennett, *IEEE J. Quantum Electron.* **23**, 123 (1987).
- ¹³Q. Xu and M. Lipson, *Opt. Lett.* **31**, 341 (2006).
- ¹⁴T. J. Johnson, M. Borselli, and O. Painter, *Opt. Express* **14**, 817 (2006).
- ¹⁵The mode index is related to the bulk refractive index, n , via $n_{\text{eff}} = \beta_m/k = n \cos(\Theta)$. Here, $\beta_m = m/R$ is the mode propagation constant in the ring of radius R , k is the wave number, and Θ is the bounce angle of the modes of a “mirror” waveguide. Therefore, the pump-induced variation of the mode index, n_{eff} , should be proportional to the one of the bulk material as $n = n_{\text{eff}}/\cos(\Theta)$ [note that $\cos(\Theta)$ lies between 1 and $1/n$]. Thus, considering that the bulk SRO refractive index at the mode wavelength is $n \approx 1.8$, its modulation Δn may vary between Δn_{eff} and $1.8 \times \Delta n_{\text{eff}}$.
- ¹⁶G. V. Prakash, M. Cazzanelli, Z. Gaburro, L. Pavesi, F. Iacona, G. Franzò, and F. Priolo, *J. Appl. Phys.* **91**, 4607 (2002).
- ¹⁷R. Spano, N. Daldosso, M. Cazzanelli, L. Ferraioli, L. Tartara, J. Yu, V. Degiorgio, E. Jordana, J. M. Fedeli, and L. Pavesi, *Opt. Express* **17**, 3941 (2009).
- ¹⁸S.-Y. Seo, J. Lee, J. H. Shin, E.-S. Kang, and B.-S. Bae, *Appl. Phys. Lett.* **85**, 2526 (2004).
- ¹⁹We have used $\rho = 2.25 \times 10^{-3} \text{ kg cm}^{-3}$, $C = 1052 \text{ J kg}^{-1} \text{ K}^{-1}$, and $\tau_T \sim 1 \mu\text{s}$, which are averages between the SiO_2 and Si values weighted by the Si content in the SRO.
- ²⁰We have used $\sigma_{\text{exc}} = 2 \times 10^{-17} \text{ cm}^2$ (this work, fitted-data in Fig. 5), $N_0 = 1 \times 10^{19} \text{ cm}^{-3}$ (from Ref. 21), $\tau \sim 20 \mu\text{s}$ (from Ref. 7), and $C_A = 1 \times 10^{-31} \text{ cm}^6 \text{ s}^{-1}$ (from Ref. 21).
- ²¹A. Pitanti, D. Navarro-Urrios, N. Prtljaga, N. Daldosso, F. Gourbilleau, R. Rizk, B. Garrido, and L. Pavesi, *J. Appl. Phys.* **108**, 053518 (2010).
- ²²R. M'ghaieth, H. Maâref, I. Mihalcescu, and J. C. Vial, *Phys. Rev. B* **60**, 4450 (1999).